Phase Transformation Synthesis of Strontium Tantalum Oxynitride-Based Heterojunction for Improved Visible Light-Driven Hydrogen Evolution

Weixuan Zeng,[†] Yuan Bian,[†] Sheng Cao,[‡] Yongjin Ma,[†] Yi Liu,[†] Anquan Zhu,[†] Pengfei Tan,[†] and Jun Pan*,[†]
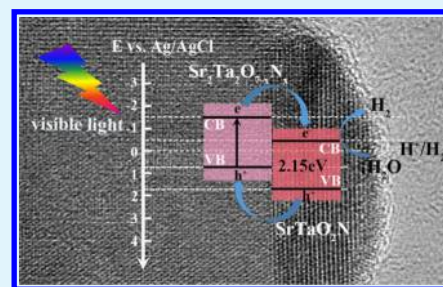
[†]Skate Key Laboratory for Powder Metallurgy, Central South University, Changsha 410083, P. R. China

[‡]Department of Chemical and Biomolecular Engineering, National University of Singapore, 10 Kent Ridge Crescent, Singapore 119260, Singapore

S Supporting Information

ABSTRACT: Tantalum oxynitride-based materials, which possess narrow band gaps and sufficient band energy potentials, have been of immense interest for water splitting. However, the efficiency of photocatalytic reactions is still low because of the fast electron−hole recombination. Here, a $Sr_2Ta_2O_{7-x}N_x$/$SrTaO_2N$ hetero-structured photocatalyst with a well-matched band structure was in situ constructed by the nitridation of hydrothermal-prepared $Sr_2Ta_2O_7$ nanosheets. Compared to $Sr_2Ta_2O_{7-x}N_x$ and pure $SrTaO_2N$, the $Sr_2Ta_2O_{7-x}N_x$/$SrTaO_2N$ heterostructured photocatalyst exhibited the highest rate of hydrogen evolution, which is ca. 2.0 and 76.4 times of $Sr_2Ta_2O_{7-x}N_x$ and pure $SrTaO_2N$, respectively, under the similar reaction condition. The enhanced performance arises from the formation of suitable band-matched heterojunction-accelerated charge separation. This work provides a promising strategy for the construction of tantalum oxynitride-based heterojunction photocatalysts.

KEYWORDS: strontium tantalum oxynitride, phase transformation, heterojunction, water splitting, hydrogen evolution

1. INTRODUCTION

Producing clean and renewable energy has been on the agenda for decades to tackle the global crisis of energy and environmental issues. As a quintessential method of hydrogen production, photocatalytic splitting of water using a semiconductor photocatalyst is one of the attractive approaches to transform the abundant solar energy into hydrogen fuel.[1] Over the past decades, there emerged plenty of semiconductors with attractive activities for hydrogen evolution.[2−5] In particular, tantalum oxide-based compounds with a perovskite-based structure have been reported to be of higher potential for the hydrogen generation reaction because of the sufficient band energy potentials for water splitting.[6−9] However, such highly active photocatalysts only respond to ultraviolet light irradiation.[10−12] On the basis of the fact that the visible light contributes to most of the solar energy, exploiting tantalum-based photocatalysts with wide visible light absorption for solar-to-fuel conversion is indispensable.

Nitriding has been proven to be an available way to reduce the band gap of tantalum oxides.[13−16] Specially, tantalum oxynitrides have come into focus in recent years because of their ideal band gaps and appropriate band edge positions.[17] Tantalum oxynitrides have much smaller band gaps (varying from 1.9 to 2.5 eV) than tantalum oxides, enabling the employment of the most visible light (approaches 43% of the sunlight spectrum).[18] Generally, tantalum oxynitrides are prepared by nitridation for many hours, in which ammonia as the nitrogen source is continuously passed through the precursor at high temperature (>1123 K).[19−23] For example, Li and coworkers prepared nitrogen-doped layered oxide $Sr_5Ta_4O_{15-x}N_x$ via heating $Sr_5Ta_4O_{15}$ at 1123 K for 15 h under ammonia flow, which was proven to be active under visible light.[24] It indicates the great potential of using tantalum oxynitrides as efficient hydrogen evolution photocatalysts, whereas further efforts are needed to improve the photocatalytic performances.

The fast recombination of photogenerated carriers is another issue to hinder the efficiency of hydrogen production. There is therefore a need to develop composite photocatalytic materials with high efficiency of separating the photoinduced carriers. Construction of heterojunctions in photocatalysts with matchable band gaps has been proven to be one of the most potential strategies for the preparation of advanced photocatalysts.[25−27] To date, many heterostructures have been extensively adopted for promoting the hydrogen evolution rate of tantalum-based photocatalysts, such as $MgTa_2O_{6-x}N_y$/TaON,[28] $NaTaO_3$/Ta_2O_5,[29] g-C_3N_4/$SrTa_2O_6$,[30] Ta_3N_5/$BaTaO_2N$,[31] and Ta_3N_5/NaTaON.[32] Among them, the conventional strategy to construct a heterojunction is by hybriding different materials or by in situ growth of one semiconductor onto the other base

semiconductor. The above-mentioned heterojunction is mostly based on two types of semiconductors. Another junction that is based on the homogeneous semiconductor was named as phase junction, usually formed between different phases within one same compound, such as band arrangement of rutile and anatase TiO_2,[33,34] three-phase TiO_2,[35] and phase junction CdS.[36] However, the reported heterojunctions based on tantalum oxynitrides that are formed via phase transformation of one semiconductor are relatively rare.

Inspired by the guide of previous studies on heterojunctions, herein, unlike the conventional heterojunction or phase junction, we report the development of a layered $Sr_2Ta_2O_{7-x}N_x$/$SrTaO_2N$ heterojunction by phase transformation of $Sr_2Ta_2O_7$ nanosheets via a thermal ammonalysis process. In addition, we choose nanostructured $Sr_2Ta_2O_7$ as the precursor in the synthesis process, which greatly decreased the ammonia-treated time. Compared to $Sr_2Ta_2O_{7-x}N_x$ and pure $SrTaO_2N$, the $Sr_2Ta_2O_{7-x}N_x$/$SrTaO_2N$ heterojunction presented improved photocatalytic activity under visible light. The promoted photocatalytic water-splitting performance could be ascribed to the matchable band gaps between $Sr_2Ta_2O_{7-x}N_x$ and $SrTaO_2N$ that boosted charge separation and transfer across the heterojunction interfaces. The present work provides an effective strategy toward the improvement of visible light-driven hydrogen evolution.

2. EXPERIMENTAL SECTION

2.1. Materials and Reagents. Ta_2O_5 (99.99%), $Sr(NO_3)_2$ (99.5%), and NaOH were used for the preparation of $Sr_2Ta_2O_7$ nanosheets. $H_2PtCl_6·6H_2O$ (99.5%) was employed as the precursor for the reduction of cocatalysts. CH_3OH (99.5%) was used as a sacrificial electron donor. All chemicals were purchased from Aladdin and used without further purification.

2.2. Sample Preparation. $Sr_2Ta_2O_7$ nanosheets were prepared by a hydrothermal method according to the process that was previously reported.[37] Ta_2O_5, $Sr(NO_3)_2$, and NaOH were added into deionized water under stirring, and then the mixture was stirred further for 2 h to ensure that the powder is fully dissolved. After that, the homogeneous mixture was poured into a 50 mL Teflon-lined autoclave. The autoclave was tightened and heated to 533 K for 72 h. After being cooled to room temperature, the obtained white products were poured into a centrifuge tube, rinsed five times with deionized water, and then dried at 333 K for 8 h. Finally, the products were ground into powders.

A series of strontium tantalum oxynitrides were obtained by heating $Sr_2Ta_2O_7$ nanosheets at 1183 K for 1 h and simply tuned by controlling the ultrapure ammonia (99.999%) flow rate (10, 15, and 20 mL s^{-1}). It is noteworthy that tantalum oxynitrides were obtained by nitridation for many hours in general; however, the nanostructured precursor could greatly reduce the ammonia-treated time in this work. Typically, 1.0 g of as-synthesized $Sr_2Ta_2O_7$ powders was placed on an alundum crucible, heated to 1183 K under flowing ultrapure ammonia at the rate of 8 K min^{-1}, and then held for 60 min. After being cooled down to room temperature, the powders were stored for use.

In this work, we deposited cocatalysts by an impregnation method and subsequent H_2 reduction.[31] Generally, 0.2 g of the as-obtained products was weighed and poured into a small beaker, and then 2 mL of H_2PtCl_6 aqueous solution (10 mg mL^{-1}) was added under ultrasonic conditions and held for 5 min. After that, the beaker was placed in a thermostatic water bath, and the temperature was controlled at 353 K. Until the solution was entirely evaporated, the resulting product was put into an alumina crucible. Finally, the product was placed in a tube furnace under the reduction atmosphere (5% H_2/Ar, 200 mL min^{-1}) at 623 K for 1 h.

2.3. Characterization. The X-ray diffraction (XRD) patterns were examined using a Rigaku D/Max 2550 powder diffractometer with Cu Kα radiation at a scan rate of 10° min^{-1}. A Nova Nano 230 scanning electron microscope and a JEM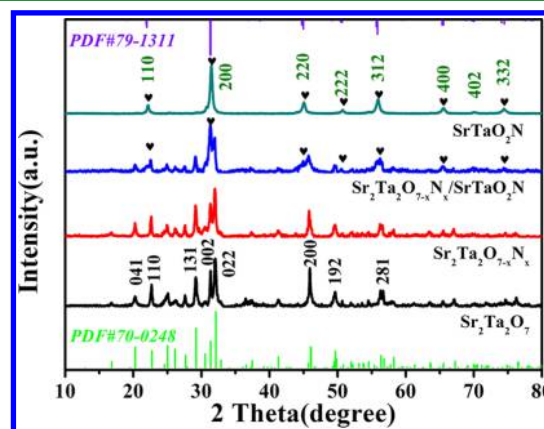-2100F field emission transmission electron microscope were employed for the characterization of the morphology of samples. Surface states of samples were analyzed by X-ray photoelectron spectroscopy (XPS, ESCALAB 250Xi), and all binding energies were corrected with the C 1s peak (284.8 eV). The UV−vis diffuse reflectance spectra of samples were recorded in the range of 200−900 nm on an Evolution 220 UV−visible spectropho-tometer (Thermo Scientific), and $BaSO_4$ was used as the reference. The time-resolved fluorescence spectra were collected using a FLS980 Series of Fluorescence Spectrometer (Edinburgh Instruments).

2.4. Photocatalytic Reactions. The water-splitting experiment was measured in a closed gas recirculation system equipped with a quartz reactor and connected to an evacuation pump. Representatively, 100 mg photocatalyst was dispersed in 100 mL 15 vol % methanol aqueous solution with continuous stirring. The above suspension was irradiated under visible light for 5 h, while the visible light source was simulated by a 300 W Xe lamp equipped with a cutoff filter ($\lambda \geq 420$ nm). The reaction temperature is kept at 279 K by using a circulating water system. The amount of hydrogen evolution was quantified by an online gas chromatography, in which a flow of nitrogen at a rate of 100 mL min^{-1} was used as the carrier gas.

2.5. Photoelectrochemical Analysis. Photoelectrochemical test was performed on an electrochemical workstation (CHI660e, China) in a standard three-electrode system (an Ag/AgCl reference electrode, a platinum sheet counter electrode, and a working electrode that was made of as-prepared photocatalysts). Na_2SO_4 aqueous solution (0.5 M, pH = 8.5) was used as the electrolyte. The test was carried out under light irradiation (300 W Xe lamp, $\lambda \geq 420$ nm). The working electrodes were fabricated in the following steps: 20 mg photocatalyst was dispersed in 1500 μL ethanediol that contained 50 μL Nafion aqueous solution, and then the solution was fully stirred. Next, 100 μL of the above slurry was dropped on a fluorine-doped tin oxide (1 cm × 1 cm) conducting glass and then annealed for 2 h in a vacuum oven at 473 K.
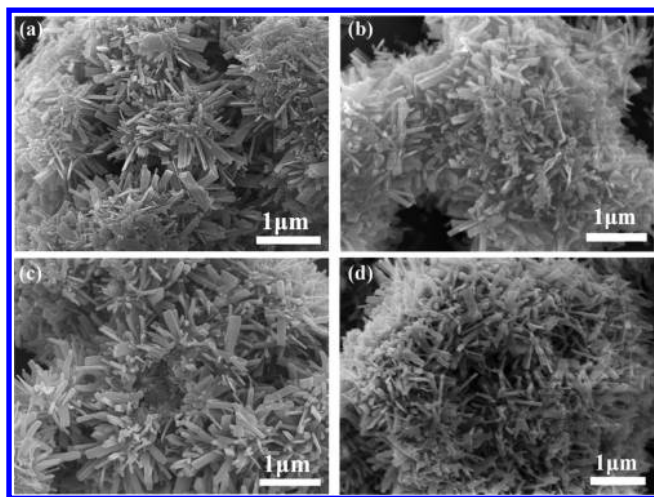
3. RESULTS AND DISCUSSION

According to the XRD patterns in Figure 1, all the peaks of the hydrothermal-prepared sample can be assigned to the

Figure 1. XRD patterns of hydrothermal-prepared $Sr_2Ta_2O_7$ and samples prepared under different ammonia flow rates (from bottom to top: untreated, 10, 15, 20 mL s^{-1}).

orthorhombic $Sr_2Ta_2O_7$ (ICDD PDF 70-0248). The other samples were obtained by heating $Sr_2Ta_2O_7$ nanosheets at the ammonia flow rate of 10, 15, and 20 mL s^{-1}. When the nitrogen flow rate was set at 10 mL s^{-1}, the XRD pattern demonstrated that the ammonia-treated process almost has no effect on the crystal structure of $Sr_2Ta_2O_7$, denoted as $Sr_2Ta_2O_{7-x}N_x$. With the ammonia flow rate increased to 15 mL s^{-1}, besides the major phase of $Sr_2Ta_2O_7$, the diffraction peak at the original (002) peak position of $Sr_2Ta_2O_7$ became sharp and intense, indicating the presence of $SrTaO_2N$, and the peak can be indexed to the (200)

Figure 2. Scanning electron microscopy (SEM) images of (a) $Sr_2Ta_2O_7$; (b) $Sr_2Ta_2O_{7-x}N_x$; (c) $Sr_2Ta_2O_{7-x}N_x/SrTaO_2N$; and (d) $SrTaO_2N$.

plane of $SrTaO_2N$ (ICDD PDF 79-1311). It means that a part of the sample was transformed from $Sr_2Ta_2O_{7-x}N_x$ to $SrTaO_2N$, indicating the formation of a $Sr_2Ta_2O_{7-x}N_x/SrTaO_2N$ hetero-structure. As the ammonia flow rate further increased (20 mL s^{-1}), the three typical peaks located at 31.38°, 44.94°, and 55.88° corresponded to the (200), (220), and (312) facets of tetragonal $SrTaO_2N$, indicating that the sample completely transformed to $SrTaO_2N$.

Figure 2 displays the morphologies of the as-prepared samples. From Figure 2a, the hydrothermal-prepared precursor $Sr_2Ta_2O_7$ rendered a flower-like structure that is consisted of nanosheets. The morphology of samples after being treated with ammonia is shown in Figure 2b–d. The flower-like structures are preserved in those samples. The morphologies of isolated sheets were also measured, as shown in Figure S1 (Supporting Information). As the flow rate increased, the edge of the nanosheet became mellow and the surface became rough, revealing the influence of nitridation on morphology.
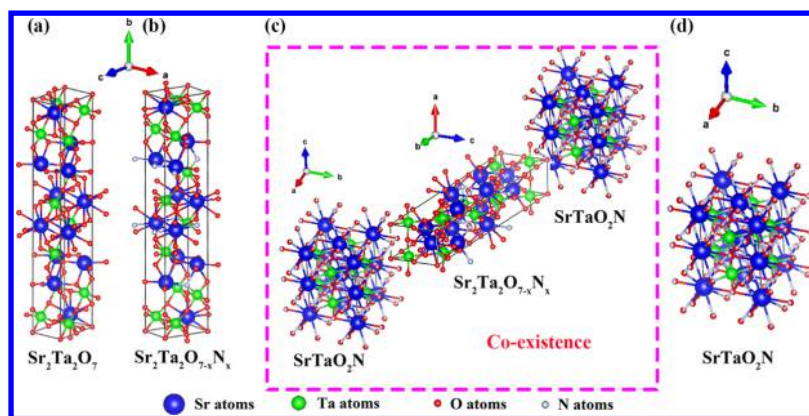
Scheme 1 illustrates the process of $Sr_2Ta_2O_7$ transformed to $SrTaO_2N$. Pristine $Sr_2Ta_2O_7$ presented an orthorhombic phase. With the increase of flow rate of ammonia, the sample retains the orthorhombic phase at first, and then $SrTaO_2N$ with the tetragonal phase appears and gradually transforms into pure tetragonal $SrTaO_2N$. Especially, when the ammonia flow rate was set as 15 mL s^{-1}, as displayed in Scheme 1c, coexistence of

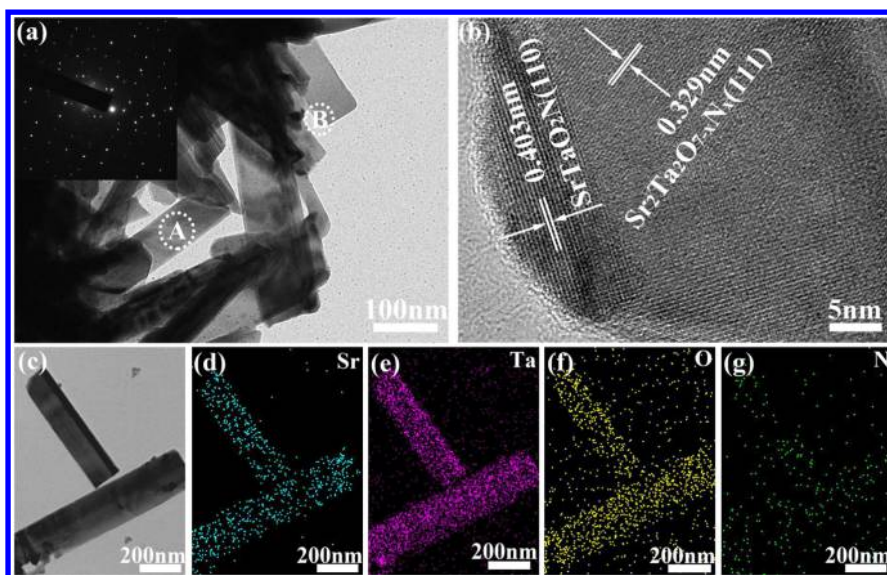orthorhombic $Sr_2Ta_2O_{7-x}N_x$ and tetragonal $SrTaO_2N$ is revealed.

Further transmission electron microscopy (TEM) analysis also convinced the coexistence of orthorhombic $Sr_2Ta_2O_{7-x}N_x$ and tetragonal $SrTaO_2N$ (Figure 3). From Figure 3a, it could be seen that a great part of the as-obtained sample showed the original morphology. The selected area electron diffraction (SAED) pattern of the area marked A was displayed in the inset of Figure 3a. Compared to pure $Sr_2Ta_2O_7$ (Figure S2a, Supporting Information), part of spots are not regularly distributed in this pattern, which can be indexed to tetragonal $SrTaO_2N$ (Figure S3c, Supporting Information), while the regular spots are related to orthorhombic $Sr_2Ta_2O_{7-x}N_x$ (Figure S3c, Supporting Information). A typical high-resolution TEM (HRTEM) image obtained by enlarging the area labeled as B was displayed in Figure 3b. Two typical lattice planes correspond to orthorhombic $Sr_2Ta_2O_{7-x}N_x$ and tetragonal $SrTaO_2N$. The distance of 0.329 nm between two adjacent fringes corresponds to the (111) plane of orthorhombic $Sr_2Ta_2O_{7-x}N_x$. Besides, the lattice spacing with a distance of 0.403 nm corresponds to the (110) plane of tetragonal $SrTaO_2N$, proving that the $Sr_2Ta_2O_{7-x}N_x/SrTaO_2N$ hetero-structure was obtained. Figure 3d–g shows the distribution of the Sr, Ta, O, and N elements within two nanosheets, suggesting homogeneous spatial distributions throughout the nanosheet body. It should be pointed out that the $Sr_2Ta_2O_{7-x}N_x/SrTaO_2N$ heterojunction herein is distinct from other conventional heterojunctions and that $SrTaO_2N$ was in situ generated on $Sr_2Ta_2O_{7-x}N_x$, resulting in the formation of an intimate interfacial contact. Thus, it would benefit to the passivation of interfacial dangling bonds and decrease the defect density, which can enable more efficient charge separation.
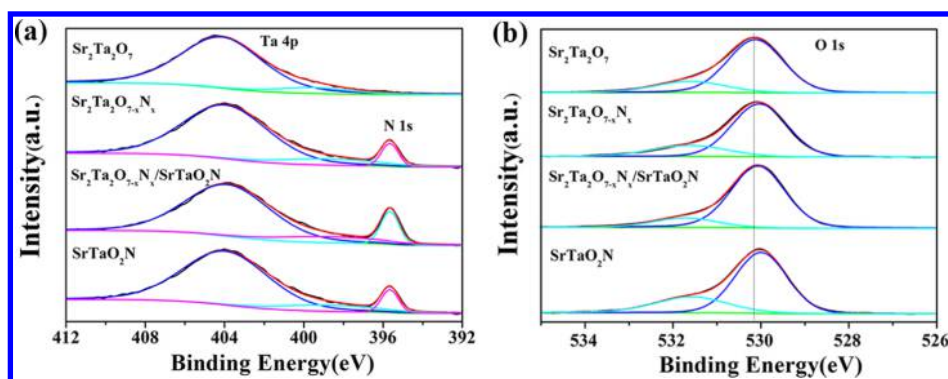
XPS analysis was employed to investigate the chemical states of pure $Sr_2Ta_2O_7$, $Sr_2Ta_2O_{7-x}N_x$, $Sr_2Ta_2O_{7-x}N_x/SrTaO_2N$, and pure $SrTaO_2N$. The high-resolution XPS spectra of N 1s and O 1s are displayed in Figure 4. In Figure 4a, the strong peak located at ca. 404.44 eV of the $Sr_2Ta_2O_7$ sample could be attributed to Ta 4p. Otherwise, no evident peak assigned to the nitrogen species can be observed for the pristine $Sr_2Ta_2O_7$, while the new peak signals at ca. 395.69, 395.64, and 395.64 eV were obtained from the thermal ammonia-treated samples, indicating that the N element exists in those samples. The peak at around ca. 395.6 eV can be ascribed to β-N, which has been confirmed by a great deal of research studies,[8,13,19] suggesting that the nitrogen is doped into the network of Ta−O−Ta and that Ta−N bonds are formed. From Figure 4b, it can be observed that the high-

Scheme 1. Structure Transition Process of $Sr_2Ta_2O_7$ with Increased Ammonia Flow Rate

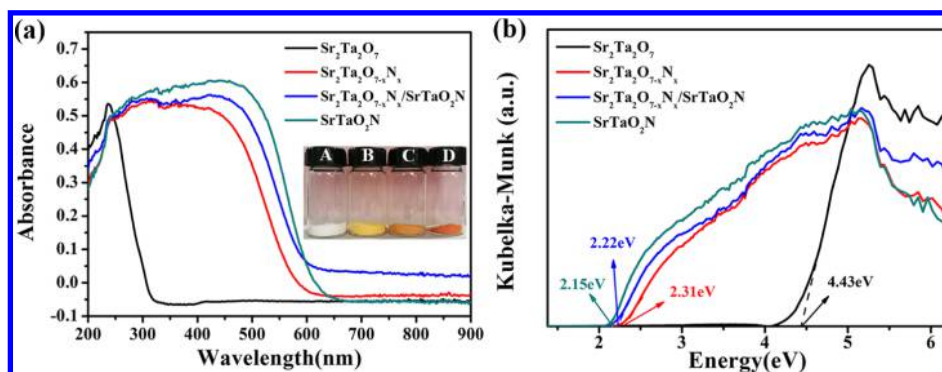**Figure 3.** (a) TEM image of $Sr_2Ta_2O_{7-x}N_x/SrTaO_2N$ nanosheets [inset: SAED pattern of the section marked A in (a)]; (b) HRTEM image of the section marked B in (a); (c) scanning TEM (STEM) image of $Sr_2Ta_2O_{7-x}N_x/SrTaO_2N$ nanosheets; (d−g) elemental mappings of Sr, Ta, O, and N within the area of (c).

Figure 4. High-resolution XPS spectra of (a) N 1s and (b) O 1s.

Figure 5. (a) UV−vis diffuse reflectance spectra of pure $Sr_2Ta_2O_7$, $Sr_2Ta_2O_{7-x}N_x$, $Sr_2Ta_2O_{7-x}N_x/SrTaO_2N$, and $SrTaO_2N$; the inset is the digital photograph of $Sr_2Ta_2O_7$ and oxynitrides [(A) $Sr_2Ta_2O_7$, (B) $Sr_2Ta_2O_{7-x}N_x$, (C) $Sr_2Ta_2O_{7-x}N_x/SrTaO_2N$, (D) $SrTaO_2N$] and (b) estimated band gaps of different samples.

resolution spectrum of O 1s is fitted into two peaks: the peak at around ca. 530 eV belongs to the Ta−O bonds and the other could be attributed to the OH group and H_2O that were adsorbed on the surface of catalysts. The O 1s spectra of ammonia-treated samples are shifted to the lower position compared with that of $Sr_2Ta_2O_7$, suggesting the decrease in the Ta−O bond and the formation of the Ta−N bond.

Figure 5a shows the UV−vis absorption spectra of $Sr_2Ta_2O_7$, $Sr_2Ta_2O_{7-x}N_x$, $Sr_2Ta_2O_{7-x}N_x/SrTaO_2N$, and $SrTaO_2N$. With the increase of ammonia flow rate, a significant red shift was found in the oxynitrides, and the absorption spectrum extends from the ultraviolet to visible region. The color of these powders changed from white to reddish orange (inset of Figure 5a), and the extended visible light absorption and phase transformation
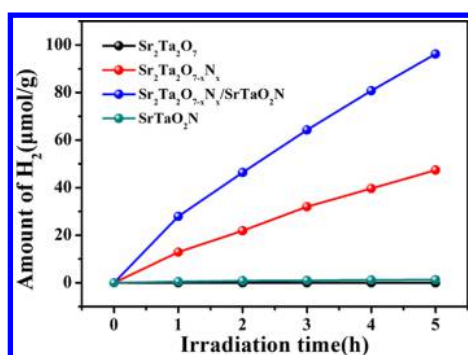
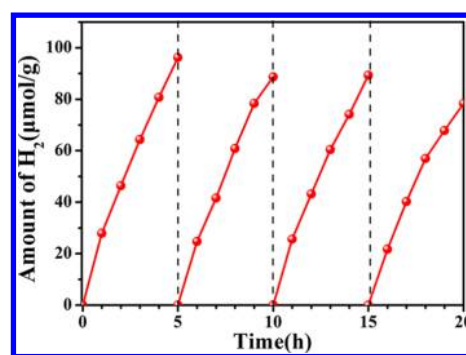**Figure 6.** Photocatalytic H_2 production activity of different samples.

Figure 8. Recycling tests of $Sr_2Ta_2O_{7-x}N_x/SrTaO_2N$ for photocatalytic H_2 evolution.

are also presented. From the Kubelka−Munk function, the band gap of pure orthorhombic $Sr_2Ta_2O_7$ is estimated to be ca. 4.43 eV (Figure 5b), and the pure tetragonal $SrTaO_2N$ has a band gap of ca. 2.15 eV. The band gaps of $Sr_2Ta_2O_{7-x}N_x$ and $Sr_2Ta_2O_{7-x}N_x/SrTaO_2N$ are estimated to be ca. 2.31 and 2.22 eV, respectively. This extended visible light absorption greatly improves the utilization of the sunlight. The band edge positions of those samples were also evaluated by combining the Mott−Schottky plots (Figure S5, Supporting Information). All the samples proved to be n-type semiconductors, and the potentials of conduction bands can be calculated as ca. −1.78, −1.78, −0.88, and −0.64 eV. To combine with the band gap values estimated from the UV−vis spectra (Figure 5), the valence band (VB) maximum of those samples should be located at 2.65, 0.53, 1.34, and 1.51 eV. Compared to $Sr_2Ta_2O_7$, $Sr_2Ta_2O_{7-x}N_x$ shows an obvious upward shift in VB maximum, as a result of the N 2p blend with O 2p orbitals, which is reported in previous studies.[14,18,26]

The photocatalytic hydrogen evolution amounts of those samples were measured under visible light irradiation, using the composites loaded with Pt as cocatalysts in aqueous solutions in which methanol acts as a sacrificial electron donor. As shown in Figure 6, $Sr_2Ta_2O_7$ cannot produce hydrogen, and the hydrogen evolution amounts of $Sr_2Ta_2O_{7-x}N_x$, $Sr_2Ta_2O_{7-x}N_x/SrTaO_2N$, and $SrTaO_2N$ under visible light irradiation were evaluated to be ca. 47.37, 96.29, and 1.26 μmol g^{-1}, respectively, in the first 5 h. Especially, the $Sr_2Ta_2O_{7-x}N_x/SrTaO_2N$ heterojunction exhibits the highest rate of hydrogen evolution, which is ca. 2.0 and 76.4 times of pure $Sr_2Ta_2O_{7-x}N_x$ and $SrTaO_2N$, respectively, under the similar reaction condition.

On the basis of differences in band gap and the position of conduction band between $Sr_2Ta_2O_{7-x}N_x$ and $SrTaO_2N$, the band arrangements are given in Figure 7a. The staggered gap indicated the formation of a typical type II heterojunction, which can greatly boost the separation and transfer of photogenerated electron−hole pairs.[36,38] To investigate the lifetime of photo-

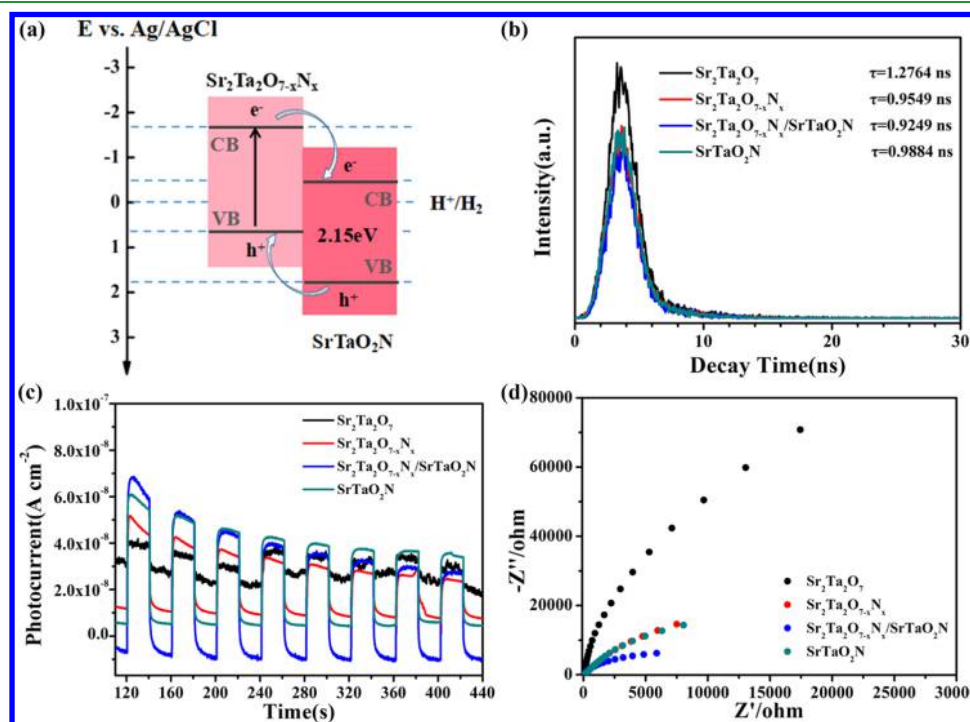**Figure 7.** (a) Estimated relative band position of the $Sr_2Ta_2O_{7-x}N_x/SrTaO_2N$ heterojunction; (b) fitting fluorescence decay curves of pure $Sr_2Ta_2O_7$, $Sr_2Ta_2O_{7-x}N_x$, $Sr_2Ta_2O_{7-x}N_x/SrTaO_2N$, and $SrTaO_2N$ recorded at the emission wavelength of 376 nm and at the excitation wavelength of 341 nm. (c) Photocurrent density and (d) EIS of as-prepared samples.

generated charge carriers, the time-resolved fluorescence spectra of all the samples were recorded (Figure 7b). The lifetimes of $Sr_2Ta_2O_7$, $Sr_2Ta_2O_{7-x}N_x$, $Sr_2Ta_2O_{7-x}N_x/SrTaO_2N$, and $SrTaO_2N$ were 1.2764, 0.9549, 0.9249, and 0.9884 ns, respectively. The $Sr_2Ta_2O_{7-x}N_x/SrTaO_2N$ sample exhibits the lowest fluorescence decay time compared to other samples, indicating that the electrons in the conduction band of $Sr_2Ta_2O_{7-x}N_x$ can transfer to the conduction band of $SrTaO_2N$ rapidly, which facilitates charge carrier separation. Thus, the formation of heterojunctions accelerated the separation and transfer of photoexcited charge carriers. Moreover, photocurrent responses confirmed the significant effect of charge separation and migration in photocatalytic performance (Figure 7c). Pure $Sr_2Ta_2O_7$ exhibits the lowest photocurrent density because of the fast recombination of photogenerated carriers. The highest photocurrent obtained by $Sr_2Ta_2O_{7-x}N_x/SrTaO_2N$ could be ascribed to the heterostructure, which is beneficial to the charge transfer and separation. Furthermore, the charge separation processes can be confirmed again from the electrochemical impedance spectroscopy (EIS) tests. As displayed in Figure 7d, $Sr_2Ta_2O_{7-x}N_x/SrTaO_2N$ exhibited a smaller radius compared with other samples. As known, a smaller radius of EIS Nyquist plot refers to a lower charge-transfer resistance, suggesting a decreased interfacial charge-transfer resistance in $Sr_2Ta_2O_{7-x}N_x/SrTaO_2N$. The result further proves that the formation of the $Sr_2Ta_2O_{7-x}N_x/SrTaO_2N$ heterojunction could remarkably enhance the efficiency of charge separation and migration.

The stability of the photocatalyst is another important factor to evaluate the photocatalytic activity. It is common that self-oxidation and reverse reaction make tantalum-based photocatalysts unstable. In this work, the recycling test for hydrogen evolution was carried out under the same experimental condition, and the results are shown in Figure 8. No apparent deactivation was observed in the four cycles of hydrogen evolution reaction. In addition, from the SEM and XRD analyses (Figures S6 and S7, Supporting Information) of the $Sr_2Ta_2O_{7-x}N_x/SrTaO_2N$ sample, the phase and structure almost have no change after four cycles, indicating that $Sr_2Ta_2O_{7-x}N_x/SrTaO_2N$ is relatively stable in visible light photocatalytic hydrogen evolution.

4. CONCLUSIONS

In summary, we have successfully in situ constructed $Sr_2Ta_2O_{7-x}N_x/SrTaO_2N$ heterostructured photocatalyst via phase transformation of $Sr_2Ta_2O_7$ nanosheets. The heterojunctions have a narrow band gap and a suitable band structure for the water reduction reaction. The photocatalytic performance of this heterojunction is significantly enhanced, which is 2.0 times higher than that of $Sr_2Ta_2O_{7-x}N_x$ and 76.4 times higher than that of $SrTaO_2N$ under visible light irradiation. The promotion of photocatalytic performance is mainly attributed to the matched energy band structure between $Sr_2Ta_2O_{7-x}N_x$ and $SrTaO_2N$ phases and the favorable interfacial charge transport, accelerating photoinduced carrier separation. The present work provides a simple design strategy that can be applied to fabricate other tantalum oxynitride-based heterostructured photocatalysts with more efficient charge separation for high-efficiency solar water splitting.

ASSOCIATED CONTENT

ⓢ Supporting Information

The Supporting Information is available free of charge on the ACS Publications website at DOI: 10.1021/acsami.8b04837.

SEM images of isolated sheets: $Sr_2Ta_2O_7$, $Sr_2Ta_2O_{7-x}N_x$, $Sr_2O_{7-x}N_x/SrTaO_2N$, and $SrTaO_2N$; TEM image of $Sr_2Ta_2O_7$ nanosheets, typical HRTEM image, corresponding pattern, and elemental mappings of Sr, Ta, and O; TEM and STEM images of $SrTaO_2N$ nanosheets, typical HRTEM image, corresponding pattern, and elemental mappings of Sr, Ta, O, and N; typical TEM and STEM images of $Sr_2Ta_2O_{7-x}N_x$, corresponding pattern, and elemental mappings of Sr, Ta, O, and N; Mott–Schottky plots of $Sr_2Ta_2O_7$, $Sr_2Ta_2O_{7-x}N_x$, $Sr_2O_{7-x}N_x/SrTaO_2N$, and $SrTaO_2N$; SEM images of $Sr_2Ta_2O_{7-x}N_x/SrTaO_2N$ samples before and after four cycles; and XRD patterns of the $Sr_2Ta_2O_{7-x}N_x/SrTaO_2N$ sample before and after four cycles (PDF)

AUTHOR INFORMATION

Corresponding Author
*E-mail: jun.pan@csu.edu.cn.

ORCID Ⓘ
Sheng Cao: 0000-0002-6203-9088
Jun Pan: 0000-0002-5454-5554

Notes
The authors declare no competing financial interest.

REFERENCES

(1) Zou, Z.; Ye, J.; Sayama, K.; Arakawa, H. Direct Splitting of Water under Visible Light Irradiation with an Oxide Semiconductor Photocatalyst. *Nature* **2001**, *414*, 625−627.

(2) Hisatomi, T.; Kubota, J.; Domen, K. Recent Advances in Semiconductors for Photocatalytic and Photoelectrochemical Water Splitting. *Chem. Soc. Rev.* **2014**, *43*, 7520−7535.

(3) Zhou, C.; Zhao, Y.; Shang, L.; Shi, R.; Wu, L.-Z.; Tung, C.-H.; Zhang, T. Facile Synthesis of Ultrathin $SnNb_2O_6$ Nanosheets towards Improved Visible-Light Photocatalytic H_2-Production Activity. *Chem. Commun.* **2016**, *52*, 8239−8242.

(4) Zhao, H.; Ding, X.; Zhang, B.; Li, Y.; Wang, C. Enhanced Photocatalytic Hydrogen Evolution Along with Byproducts Suppressing over Z-scheme $Cd_xZn_{1-x}S/Au/g$-C_3N_4 Photocatalysts under Visible Light. *Sci. Bull.* **2017**, *62*, 602−609.

(5) Yu, H.; Shi, R.; Zhao, Y.; Bian, T.; Zhao, Y.; Zhou, C.; Waterhouse, G. I. N.; Wu, L.-Z.; Tung, C.-H.; Zhang, T. Alkali-Assisted Synthesis of Nitrogen Deficient Graphitic Carbon Nitride with Tunable Band Structures for Efficient Visible-Light-Driven Hydrogen Evolution. *Adv. Mater.* **2017**, *29*, 1605148.

(6) Xu, T.-G.; Zhang, C.; Shao, X.; Wu, K.; Zhu, Y.-F. Monomolecular-Layer $Ba_5Ta_4O_{15}$ Nanosheets: Synthesis and Investigation of Photocatalytic Properties. *Adv. Funct. Mater.* **2006**, *16*, 1599−1607.

(7) Sun, J.; Chen, G.; Li, Y.; Jin, R.; Wang, Q.; Pei, J. Novel (Na, K)TaO_3 Single Crystal Nanocubes: Molten Salt Synthesis, Invariable Energy Level Doping and Excellent Photocatalytic Performance. *Energy Environ. Sci.* **2011**, *4*, 4052.

(8) Mukherji, A.; Seger, B.; Lu, G. Q.; Wang, L. Nitrogen Doped $Sr_2Ta_2O_7$ Coupled with Graphene Sheets as Photocatalysts for

Increased Photocatalytic Hydrogen Production. *ACS Nano* **2011**, *5*, 3483−3492.

(9) Li, Y.; Chen, S.; He, H.; Zhang, Y.; Wang, C. Tuning Activities of $K_{1.9}Na_{0.1}Ta_2O_{6.2}H_2O$ Nanocrystals in Photocatalysis by Controlling Exposed Facets. *ACS Appl. Mater. Interfaces* **2013**, *5*, 10260−10265.

(10) Kudo, A.; Kato, H.; Nakagawa, S. Water Splitting into H_2 and O_2 on New $Sr_2M_2O_7$ (M = Nb and Ta) Photocatalysts with Layered Perovskite Structures: Factors Affecting the Photocatalytic Activity. *J. Phys. Chem. B* **2000**, *104*, 571−575.

(11) Yoshino, M.; Kakihana, M.; Cho, W. S.; Kato, H.; Kudo, A. Polymerizable Complex Synthesis of Pure $Sr_2Nb_xTa_{2-x}O_7$ Solid Solutions with High Photocatalytic Activities for Water Decomposition into H_2 and O_2. *Chem. Mater.* **2002**, *14*, 3369−3376.

(12) Hideki, K.; Asakura, K.; Kudo, A. Highly Efficient Water Splitting into H_2 and O_2 over Lanthanum Doped $NaTaO_3$ Photocatalysts with High Crystallinity and Surface Nanostructure. *J. Am. Chem. Soc.* **2003**, *125*, 3082−3089.

(13) Mukherji, A.; Sun, C.; Smith, S. C.; Lu, G. Q.; Wang, L. Photocatalytic Hydrogen Production from Water Using N-Doped $Ba_5Ta_4O_{15}$ under Solar Irradiation. *J. Phys. Chem. C* **2011**, *115*, 15674−15678.

(14) Ida, S.; Okamoto, Y.; Matsuka, M.; Hagiwara, H.; Ishihara, T. Preparation of Tantalum-Based Oxynitride Nanosheets by Exfoliation of a Layered Oxynitride, $CsCa_2Ta_3O_{10-x}N_y$, and Their Photocatalytic Activity. *J. Am. Chem. Soc.* **2012**, *134*, 15773−15782.

(15) Chen, S.; Qi, Y.; Liu, G.; Yang, J.; Zhang, F.; Li, C. A Wide Visible-Light-Responsive Tunneled $MgTa_2O_{6-x}N_x$ Photocatalyst for Water Oxidation and Reduction. *Chem. Commun.* **2014**, *50*, 14415−14417.

(16) Wang, Y.; Zhu, D.; Xu, X. Zr-Doped Mesoporous Ta_3N_5 Microspheres for Efficient Photocatalytic Water Oxidation. *ACS Appl. Mater. Interfaces* **2016**, *8*, 35407−35418.

(17) Wei, S.; Xu, X. Boosting Photocatalytic Water Oxidation Reactions over Strontium Tantalum Oxynitride by Structural Laminations. *Appl. Catal., B* **2018**, *228*, 10−18.

(18) Zhen, C.; Chen, R.; Wang, L.; Liu, G.; Cheng, H.-M. Tantalum (Oxy)nitride Based Photoanodes for Solar Driven Water Oxidation. *J. Mater. Chem. A* **2016**, *4*, 2783−2800.

(19) Liu, G.; Niu, P.; Wang, L.; Lu, G. Q.; Cheng, H.-M. Achieving Maximum Photo-Oxidation Reactivity of $Cs_{0.68}Ti_{1.83}O_{4-x}N_x$ Photocatalysts through Valence Band Fine-tuning. *Catal. Sci. Technol.* **2011**, *1*, 222−225.

(20) Mukherji, A.; Marschall, R.; Tanksale, A.; Sun, C.; Smith, S. C.; Lu, G. Q.; Wang, L. N-Doped $CsTaWO_6$ as a New Photocatalyst for Hydrogen Production from Water Splitting Under Solar Irradiation. *Adv. Funct. Mater.* **2011**, *21*, 126−132.

(21) Pan, J.; Li, J.; Yan, Z.; Zhou, B.; Wu, H.; Xiong, X. SnO_2@CdS Nanowire-quantum Dots Heterostructures: Tailoring Optical Properties of SnO_2 for Enhanced Photodetection and Photocatalysis. *Nanoscale* **2013**, *5*, 3022−3029.

(22) Zhou, B.; Yang, S.; Wu, W.; Sun, L.; Lei, M.; Pan, J.; Xiong, X. Self-assemble SnO_2@TiO_2 Porous Nanowire-nanosheet Heterostructures for Enhanced Photocatalytic Property. *CrystEngComm* **2014**, *16*, 10863−10869.

(23) Fu, J.; Skrabalak, S. E. Enhanced Photoactivity from Single-Crystalline $SrTaO_2N$ Nanoplates Synthesized by Topotactic Nitridation. *Angew. Chem., Int. Ed.* **2017**, *129*, 14357−14361.

(24) Chen, S.; Yang, J.; Ding, C.; Li, R.; Jin, S.; Wang, D.; Han, H.; Zhang, F.; Li, C. Nitrogen-Doped Layered Oxide $Sr_5Ta_4O_{15-x}N_x$ for Water Reduction and Oxidation under Visible Light Irradiation. *J. Mater. Chem. A* **2013**, *1*, 5651−5659.

(25) Kudo, A.; Miseki, Y. Heterogeneous Photocatalyst Materials for Water Splitting. *Chem. Soc. Rev.* **2009**, *38*, 253−278.

(26) Qu, Y.; Duan, X. Progress, Challenge and Perspective of Heterogeneous Photocatalysts. *Chem. Soc. Rev.* **2013**, *42*, 2568−2580.

(27) Low, J.; Yu, J.; Jaroniec, M.; Wageh, S.; Al-Ghamdi, A. A. Heterojunction Photocatalysts. *Adv. Mater.* **2017**, *29*, 1601694.

(28) Chen, S.; Qi, Y.; Hisatomi, T.; Ding, Q.; Asai, T.; Li, Z.; Ma, S. S. K.; Zhang, F.; Domen, K.; Li, C. Efficient Visible-Light-Driven Z-Scheme Overall Water Splitting Using a $MgTa_2O_{6-x}N_y$/TaON Heterostructure Photocatalyst for H_2 Evolution. *Angew. Chem., Int. Ed.* **2015**, *54*, 8498−8501.

(29) Xu, L.; Sun, X.; Tu, H.; Jia, Q.; Gong, H.; Guan, J. Synchronous Etching-epitaxial Growth Fabrication of Facet-Coupling $NaTaO_3$/Ta_2O_5 Heterostructured Nanofibers for Enhanced Photocatalytic Hydrogen Production. *Appl. Catal., B* **2016**, *184*, 309−319.

(30) Adhikari, S. P.; Hood, Z. D.; Wang, H.; Peng, R.; Krall, A.; Li, H.; Chen, V. W.; More, K. L.; Wu, Z.; Geyer, S.; Lachgar, A. Enhanced Visible Light Photocatalytic Water Reduction from a g-C_3N_4/$SrTa_2O_6$ Heterojunction. *Appl. Catal., B* **2017**, *217*, 448−458.

(31) Qi, Y.; Chen, S.; Li, M.; Ding, Q.; Li, Z.; Cui, J.; Dong, B.; Zhang, F.; Li, C. Achievement of Visible-Light-Driven Z-Scheme Overall Water Splitting Using Barium-modified Ta_3N_5 as A H_2-evolving Photocatalyst. *Chem. Sci.* **2017**, *8*, 437−443.

(32) Hou, J.; Wu, Y.; Cao, S.; Liang, F.; Lin, Z.; Gao, Z.; Sun, L. In Situ Phase-Induced Spatial Charge Separation in Core-Shell Oxynitride Nanocube Heterojunctions Realizing Robust Solar Water Splitting. *Adv. Energy Mater.* **2017**, *7*, 1700171.

(33) Kawahara, T.; Konishi, Y.; Tada, H.; Tohge, N.; Nishii, J.; Ito, S. A Patterned TiO_2(Anatase)/TiO_2(Rutile) Bilayer-Type Photocatalyst: Effect of the Anatase/Rutile Junction on the Photocatalytic Activity. *Angew. Chem., Int. Ed.* **2002**, *114*, 2935−2937.

(34) Scanlon, D. O.; Dunnill, C. W.; Buckeridge, J.; Shevlin, S. A.; Logsdail, A. J.; Woodley, S. M.; Catlow, C. R. A.; Powell, M. J.; Palgrave, R. G.; Parkin, I. P.; Watson, G. W.; Keal, T. W.; Sherwood, P.; Walsh, A.; Sokol, A. A. Band Alignment of Rutile and Anatase TiO_2. *Nat. Mater.* **2013**, *12*, 798−801.

(35) Preethi, L. K.; Mathews, T.; Nand, M.; Jha, S. N.; Gopinath, C. S.; Dash, S. Band Alignment and Charge Transfer Pathway in Three Phase Anatase-Rutile-Brookite TiO_2 Nanotubes: An Efficient Photocatalyst for Water Splitting. *Appl. Catal., B* **2017**, *218*, 9−19.

(36) Ai, Z.; Zhao, G.; Zhong, Y.; Shao, Y.; Huang, B.; Wu, Y.; Hao, X. Phase Junction CdS: High Efficient and Stable Photocatalyst for Hydrogen Generation. *Appl. Catal., B* **2018**, *221*, 179−186.

(37) Zhou, C.; Chen, G.; Li, Y.; Zhang, H.; Pei, J. Photocatalytic Activities of $Sr_2Ta_2O_7$ Nanosheets Synthesized by a Hydrothermal Method. *Int. J. Hydrogen Energy* **2009**, *34*, 2113−2120.

(38) Yuan, Y.-P.; Ruan, L.-W.; Barber, J.; Joachim Loo, S. C.; Xue, C. Hetero-Nanostructured Suspended Photocatalysts for Solar-to-Fuel Conversion. *Energy Environ. Sci.* **2014**, *7*, 3934−3951.